Optics Communications 419 (2018) 90–96

Contents lists available at ScienceDirect

Optics Communications

journal homepage: www.elsevier.com/locate/optcom

Tunable metasurface with two non-coplanar and inter-perpendicular graphene nanoribbon arrays for the coupling between localized and delocalized surface plasmon polaritons

Ze Tao Xie [a], Feng Chao Ni [a], Qi Chang Ma [a], Jin Tao [c], Jian Li [a], Hongyun Meng [a], Xu Guang Huang [a,b,*]

[a] Guangzhou Key Laboratory for Special Fiber Photonic Devices and Applications, South China Normal University, Guangzhou 510006, People's Republic of China
[b] Provincial Key Laboratory of Nanophotonic Functional Materials and Devices, South China Normal University, Guangzhou 510006, People's Republic of China
[c] State Key Laboratory of Optical Communication Technologies and Networks, Wuhan Research Institute of Posts Telecommunications, Wuhan 430074, People's Republic of China

ARTICLE INFO

Keywords:
Surface plasmons
Metasurface
Graphene
Integrated optics devices

ABSTRACT

Graphene metasurface has attracted a lot of attentions due to the unique tunability for exotic electromagnetic properties. In this work, we propose and numerically investigate a tunable metasurface with two non-coplanar and inter-perpendicular graphene nanoribbon arrays. The variation of transmission at different substrate thickness and the coupled mode are analyzed. It is shown that the Rabi-like splitting can be achieved by the coupling between localized and delocalized graphene surface plasmon polaritons. Tunable coupling strength and positions with different gate-voltages have been discussed. The effect of relaxation time and oblique incidences to resonant responses are also investigated. Additionally, we find an optical analogue of a spring, where the spectral dip vibrates around its equilibrium position at a certain wavelength. Our study suggests that the proposed structure is potentially attractive for realization of tunable double-channel filter, optical switch, and variable optical attenuator based on the graphene metasurface.

1. Introduction

Metamaterials are new artificial three-dimensional or bulk structures with remarkable physical properties unavailable in nature. Their physical properties can be obtained by arranging a set of small scatterers or apertures in a regular pattern [1,2]. Due to the potential of manipulating light propagation and light–matter interactions, they have become a research focus over the past decade. Three-dimensional metamaterials can be shrunk into a two-dimensional structure via arranging small scatterers or apertures on an interface or a surface. This new two-dimensional structure of metamaterials is so called metasurface [3]. Due to the amplitude, phase or/and polarization of metasurfaces can be modified by patterning planar structures with subwavelength thickness, their surface or interface reflections and transmissions give rise to widespread interest in physicists and material scientists. On the contrary, effective dielectric constant and refractive index attract relatively less attention because of the minimum propagation phase which introduced by its subwavelength thickness [4–6]. Additionally, metasurface has revealed advantages of reducing losses and increasing operating bandwidth in comparison with metamaterials [7,8]. However, it is known that traditional metasurface is comprised of periodic metal–insulator or all-dielectric structures, most of these structures cannot support plasmonic response within mid-infrared or longer wavelengths, and their optical responses can only be controlled by the geometry of structures, which limits their applications.

Graphene, a two-dimensional material with unique and fantastic physical properties, has become an attractive alternative candidate for plasmonic material in terahertz and mid-infrared frequencies [9–11]. Its optical response is strongly dependent on the Fermi level relative to the Dirac point, and the Fermi level of graphene can be controlled via chemical doping, applying electrostatic or magnetostatic field [12–15]. Notably, graphene has well-known properties including dynamical tunability and strong local field enhancement [16,17]. These unique virtues have opened up new avenues for many applications, such as surface plasmonic waveguides [18], optical sensors [19], terahertz metamaterials [16], nano-imaging [20], terahertz sources and detectors [21]. The appearance of graphene has created a broader platform for the study of surface plasmon optoelectronics devices [22].

* Corresponding author.
E-mail address: huangxg@scnu.edu.cn (X.G. Huang).

https://doi.org/10.1016/j.optcom.2018.03.020
Received 24 November 2017; Received in revised form 4 March 2018; Accepted 8 March 2018

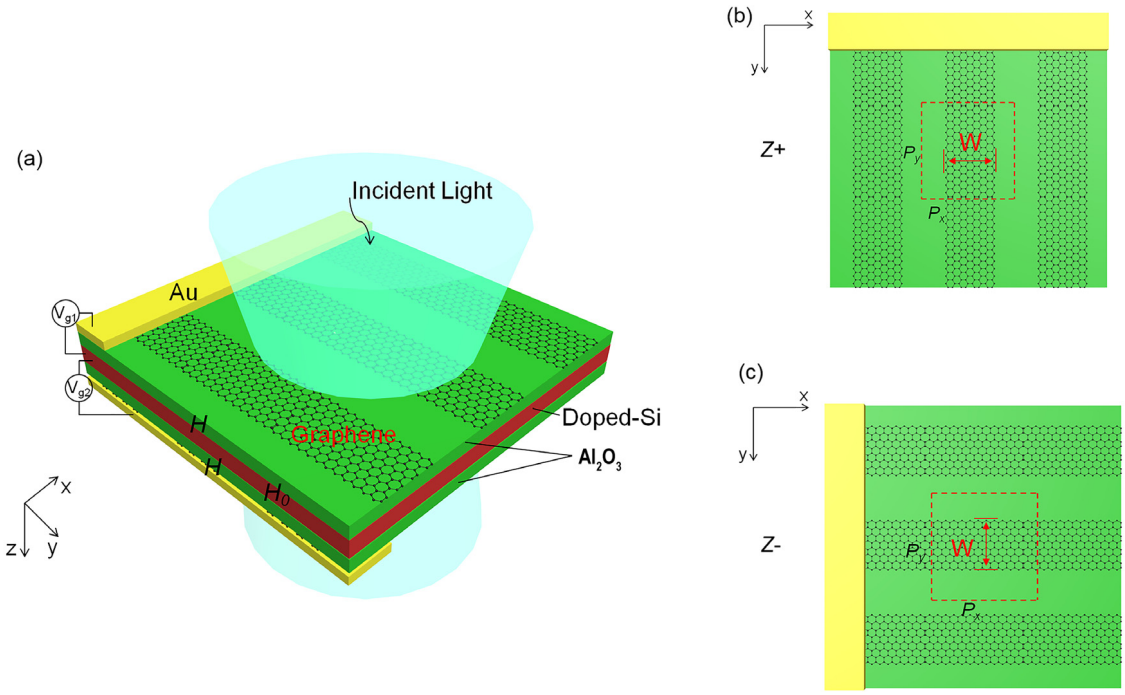

Fig. 1. (a) 3D schematic of the tunable metasurface with two non-coplanar and inter-perpendicular graphene nanoribbon arrays. The thickness of Doped-Si $H_0 = 10$ nm, and thicknesses of Al_2O_3 layers are both H. (b) The unit cell structure of our design on top layer, the periods of the x and y directions are $P_x = 300$ nm and $P_y = 300$ nm, respectively. Graphene nanoribbons width $W = 150$ nm. (b) The unit cell structure of our design on bottom layer, the periods of the x and y directions are $P_x = 300$ nm and $P_y = 300$ nm, respectively. Graphene nanoribbons width $W = 150$ nm.

So far, series of research projects on graphene metasurface have been carried out by numerous research groups. H.S. Chu et al. proposed a simple active plasmonic switching with graphene nanoribbon arraying at mid-infrared wavelengths, which shifts the transmission spectrum by changing the doping level of graphene or the number of graphene ribbon layers [23]. A graphene metasurface that can efficiently control the phase and amplitude of infrared light was demonstrated by Z.B. Li et al., and it realized reflective focusing lenses, anomalous reflection, and non-diffracting Airy beams [3]. Z.H. Chen et al. numerically investigated a gate-controlled on-chip graphene metasurface structure. Their results show that the structure as a refractive index sensor can achieve an overall figure of merit of 8.89 in infrared wavelength range [24]. Most of the previous research works were based on localized graphene surface plasmon polaritons (SPPs), however, graphene nanoribbons can also support delocalized SPPs with propagating modes such as edge modes and waveguiding modes [25,26]. Besides, the interaction between localized and delocalized SPPs based on metasurface has rarely been considered.

In this article, we propose a flexible design of metasurface with two non-coplanar and inter-perpendicular graphene nanoribbon arrays. An obvious spectral splitting, a Rabi-like splitting, namely the coupling of localized and delocalized plasmonic, is numerically investigated. We demonstrate the coupling strength of the structure depends on the separation between the two arrays. Cases of different relaxation time and oblique incidences to resonant responses are also discussed. By applying different Fermi levels, the tunability of the structure is analyzed. The results show that the spectral dip varies around its equilibrium position at a certain wavelength. Moreover, we provide a promising solution to design optical switch and variable optical attenuator based on the graphene metasurface in the mid-infrared region.

2. Design of graphene metasurface model

Based on the carrier density of graphene can be changed by chemical doping, applying external electrostatic or magnetostatic field, the tunability in graphene is achieved by changing the Fermi level E_f. Under the condition of the random-phase approximation, the dynamical optical response of graphene can be calculated from the Kubo equation, its complex surface conductivity is estimated as [18,24]:

$$\sigma(\omega) = \sigma_{\text{interband}} + \sigma_{\text{intraband}}. \tag{1}$$

The first term of the formula represents the interband transition:

$$\sigma_{\text{interband}} = \frac{e^2}{4\hbar}\left\{\frac{1}{2} + \frac{1}{\pi}\arctan\left(\frac{\hbar\omega - 2E_f}{2k_BT}\right) - \frac{i}{2\pi}\ln\left(\frac{(\hbar\omega + 2E_f)^2}{(\hbar\omega - 2E_f)^2 + (2k_BT)^2}\right)\right\}, \tag{2}$$

the second term of the formula represents the intraband transition:

$$\sigma_{\text{intraband}} = \frac{2ie^2k_BT}{\pi\hbar^2(\omega + i\tau^{-1})}\ln\left(2\cosh\left(\frac{E_f}{2k_BT}\right)\right), \tag{3}$$

here $\hbar = h/2\pi$ is the reduced Plank's constant, ω is the optical angular frequency, k_B is the Boltzmann constant, T is ambient temperature, and τ is the carrier relaxation time. According to the above formulas, the interband and intraband transitions of graphene complex surface conductivity are closely related to its Fermi level E_f and incident light frequency. The carrier concentration determines the Fermi level of doping graphene with $E_f = \hbar v_f(\pi n_g)^{1/2}$ (where v_f is Fermi velocity, n_g is carrier concentration) [27]. For $|E_f| < \hbar\omega/2$, the interband conductivity contribution becomes dominant in the total conductivity of graphene, and it can run through a wide bandwidth range from the visible spectral region to infrared region. For $|E_f| > \hbar\omega/2$, the conductivity contribution of the intraband transition is dominant, and allows graphene electrons to be excited for surface plasmons. In our simulations, we have calculated both the intraband and interband conductivity contributions of the Kubo formula.

In the theoretical calculation and numerical simulation, graphene can be equivalent to bulk material with a thickness of t_g because of its

monolayer atomic size structure. The surface conductivity $\sigma(\omega)$ can be converted into bulk conductivity:

$$\sigma_{g,V}(\omega) = \sigma(\omega)/t_g. \quad (4)$$

Based on the Ampere's law and Ohm's law in stationary regime, the effective in-plane permittivity of graphene is defined as follows [25]:

$$\varepsilon_g = \varepsilon_0 + \frac{i\sigma(\omega)}{\varepsilon_0 \omega t_g}, \quad (5)$$

where ε_g is the permittivity with real part $\varepsilon_{g,r} = \varepsilon_o - \sigma_{g,i}/(\omega t_g)$ and imaginary part $\varepsilon_{g,i} = \sigma_{g,r}/(\omega t_g)$, t_g ($t_g = 0.34$ nm [28]) is the thickness of graphene, ε_o is the permittivity in vacuum.

The designed tunable metasurface with two non-coplanar and inter-perpendicular graphene nanoribbon arrays is shown in Fig. 1(a). A doped-silicon (Doped-Si) substrate is sandwiched between two same-thickness layers of insulating medium (aluminum oxide, Al_2O_3) and is used for an electrode to support the graphene metasurface. The periodic graphene nanoribbons arrayed in y direction are deposited on the top layer of Al_2O_3, while the periodic graphene nanoribbons arrayed in x direction are deposited on the bottom layer of Al_2O_3. All of graphene nanoribbons in the two planes are composed of 5 graphene layers to enhance the modulation depth, as reported in Ref. [23]. Gold (Au) is used for electrodes to apply different voltage V_{g1} and V_{g2}. Fermi level of graphene is expressed as $E_f = \hbar v_f (\pi n_g)^{1/2}$ and carrier concentration is $n_g = \varepsilon_o \varepsilon_d V_g / eH$, where V_g is the applied voltage; ε_d ($=n_d^2$) and n_d are respectively the permittivity and refractive index of the dielectric medium (Al_2O_3); H is the thickness of insulating medium in this paper). Thus Fermi level of graphene can be tuned by changing voltage V_{g1} and V_{g2}. An x-polarized normally incident plane wave along with the $-z$ direction is utilized to excite the graphene plasmon on top layer of graphene nanoribbons. The (complex) refractive index of Al_2O_3 is obtained from Table I, page 662 in Ref. [29], which includes dispersion and absorption factors of the material. In addition, the (complex) refractive index of the P-doped Si at the doping concentration of 10^{18} cm^{-3}, obtained from Fig. 4 (Curves of the refractive index and the extinction coefficient versus wavelength) in Ref. [30], has also considered the dispersion and absorption effects in all simulations below.

In the following, the 3D finite-difference time-domain (FDTD) method (Lumerical FDTD solutions software) is used to simulate of the unit cell structure, the periodic boundary conditions are applied in the x and y directions, perfect matched layers (PML) absorbing boundary conditions are applied in the z direction. The above surface-conductivity material-mode is used to simulate the optical property of graphene and the conductivity for N-layer graphene is $N\sigma$ (number of graphene layers $N \lesssim 6$) [31,32].

3. Coupling of the metasurface with two non-coplanar and inter-perpendicular graphene nanoribbon arrays

To explore the effect of the mode coupling between two non-coplanar and inter-perpendicular graphene nanoribbon arrays, we first individually simulate and analysis the situation of the metasurface with only one layer of graphene nanoribbon array. In the simulations, Fermi level E_f of the graphene nanoribbons is set to be 0.5 eV, with the scattering probability of $\Gamma = 0.00099$ eV (corresponding to the carrier relaxation time $\tau \approx 0.33$ ps) and ambient temperature of $T = 300$ K. Thicknesses of two Al_2O_3 layers are both 40 nm and the thickness of the doped-Si is 10 nm. From the transmission spectrum [green dash line in Fig. 2(a)] of only top layer of graphene nanoribbons, a clear dip can be observed at 5.68 μm, resulting from the SPPs resonant mode of the graphene nanoribbons excited by the x-polarization incident light. However, for only bottom layer of graphene nanoribbons, the transmittance [red dot line in Fig. 2(a)] is closed to 1.0, because the SPPs mode of the graphene nanoribbons cannot be excited. Additionally, the decrease in transmittance near 2 μm is attributed to the fact that the larger absorption of graphene at shorter wavelengths. Then we

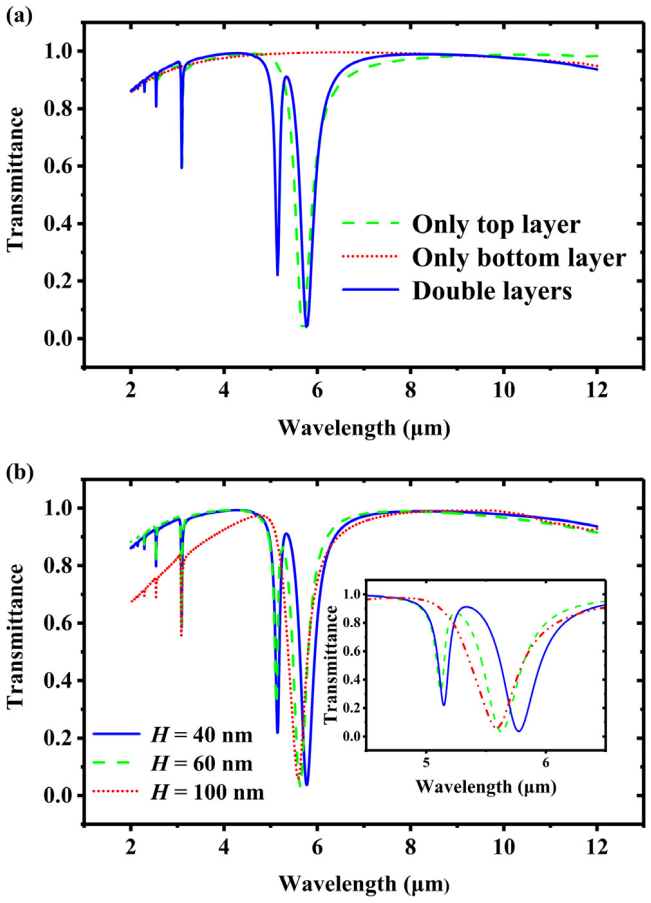

Fig. 2. (a) Transmission spectra of only top layer, only bottom layer and double layers of graphene nanoribbons. (b) Transmission spectra of the metasurface at different thicknesses of the Al_2O_3. The insert is the zooming in the wavelength of 5 μm.

simulate and analysis the metasurface with double layers of graphene nanoribbons. The transmission spectrum [blue solid line in Fig. 2(a)] displays an obvious spectral splitting with the main dip at 5.77 μm wavelength and the induced secondary dip at 5.15 μm, compared to the green dash line. Furthermore, a transmission peak appears at 5.36 μm. The result reveals that the two inter-perpendicular graphene nanoribbon arrays in different planes have been coupled each other to produce a new mode.

To further investigate the coupling of the two non-coplanar and inter-perpendicular graphene nanoribbon arrays, different thicknesses of the Al_2O_3 (different separations between the two graphene arrays) are simulated respectively. Their transmission spectra are shown in Fig. 2(b). One can see that for the thickness of $H < 100$ nm, the dip-splitting, a Rabi-like splitting, happens with one main dip and one narrow induced or secondary dip. With the further decrease of the thickness of H, the secondary dip becomes deeper, although the position of the secondary dip remains unchanged. Above phenomena can be interpreted that the interaction or the coupling between the top and bottom graphene nanoribbons occurs and increases gradually with the decrease of the separation between them. At the meantime, the positions of the main dip and the peak are both blue-shifted as increasing the separation. The main dip keeps almost constant transmittance and is toward the dip position of the only top array, but the transmittance of the transmission peak gradually decreases. It reveals the gradual weakening of the interaction between the two graphene nanoribbon arrays until the SPPs mode of the bottom graphene nanoribbons unable to be excited. Therefore, the coupling strength of the structure can be

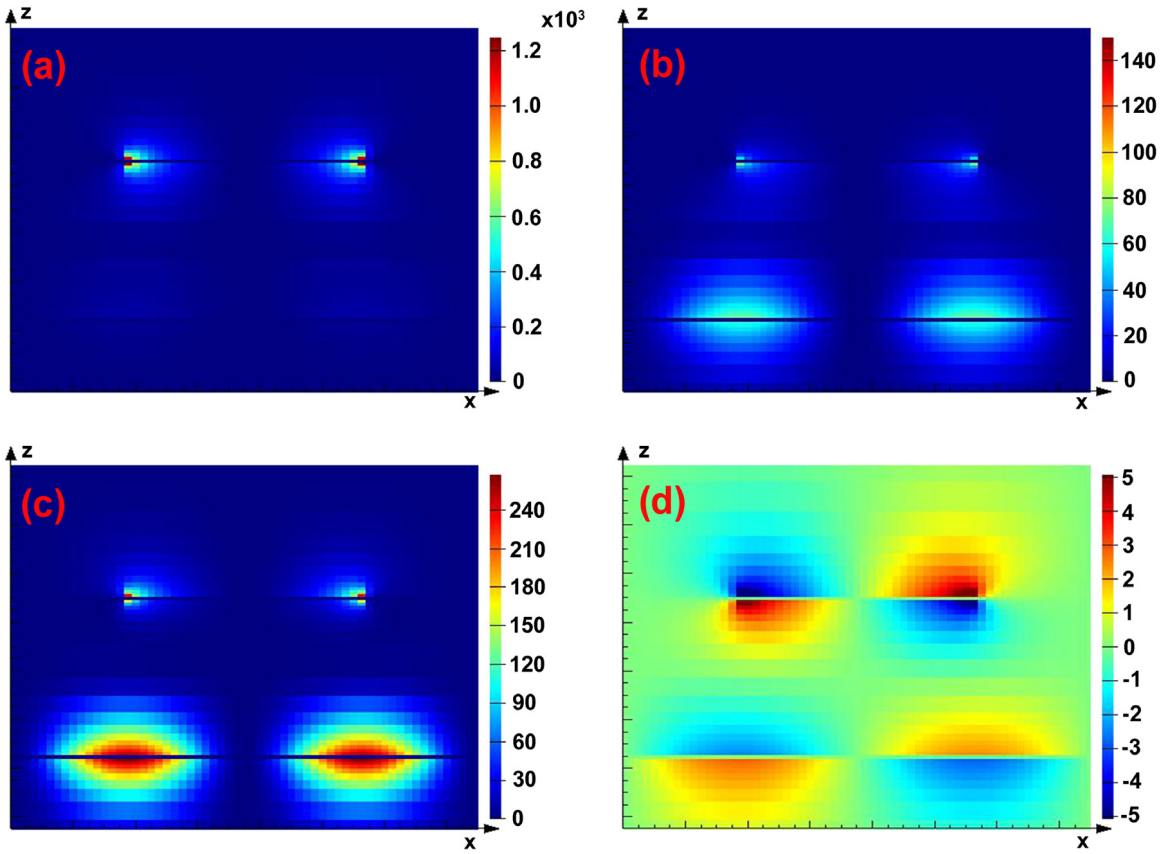

Fig. 3. The field distributions of the $|E_z|^2$-component at the main dip of 5.63 μm (a), at the transmission peak of 5.24 μm (b), and the induced dip of 5.12 μm (c), for the thickness of the Al_2O_3 of $H = 60$ nm. (d) The E_z field distribution in the x–o–z plane at the wavelength of 5.12 um.

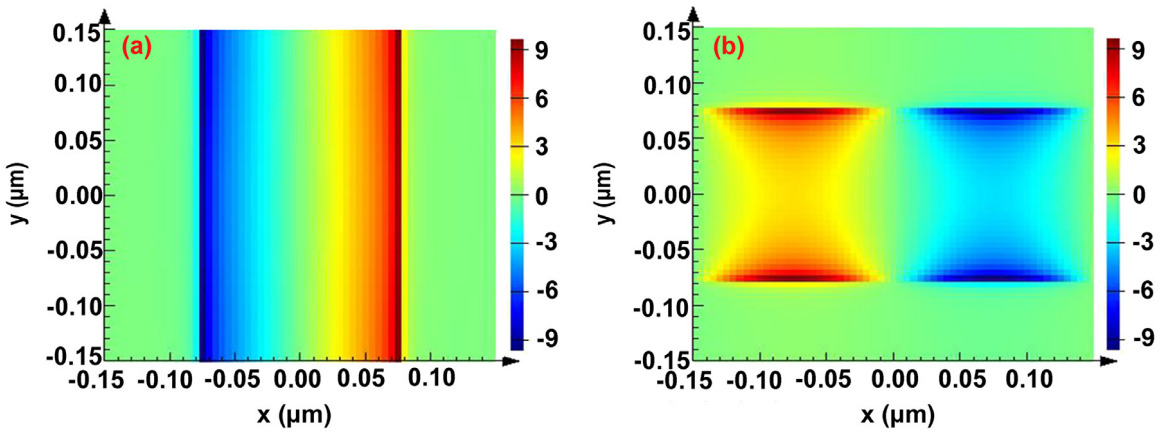

Fig. 4. The E_z field distributions of the two graphene arrays in the x–o–y plane for $\lambda = 5.12$ μm. (a) The monitor is set at 2 nm above the top graphene nanoribbons arrayed in the y-direction. (b) The monitor is set at 2 nm above the bottom graphene nanoribbons arrayed in the x-direction.

controlled by the separation between the two arrays or the thickness of the Al_2O_3.

To get more insight into the physics of the observed spectral splitting, we simulated respectively the field distributions of $|E_z|^2$-component corresponding to the main dip, the transmission peak and the secondary dip for $H = 60$ nm. As shown in Fig. 3(a), only the SPPs on the top layer of graphene nanoribbons can be excited at $\lambda = 5.63$ μm. Its light field concentrates mostly on the edges of the graphene nanoribbons and distributes along the $\pm z$ directions, corresponding to the position of the main dip, while the bottom graphene nanoribbons have nearly no field distribution. One can see in Fig. 3(b) that the plasmonic resonance of the bottom graphene nanoribbons becomes pronounced at $\lambda = 5.24$ μm and its light field is slightly overlapped with the one on the top graphene nanoribbons. Moreover, the plasmon resonance of top layer is obviously weaker, corresponding to the transmission peak in Fig. 2(a). In Fig. 3(c), at $\lambda = 5.12$ μm, the plasmonic resonance of the bottom graphene nanoribbons becomes stronger than that of the bottom graphene nanoribbons of Fig. 3(b). As a result, the secondary dip at $\lambda = 5.12$ μm is induced, as shown in Fig. 2(b). Additionally, Fig. 3(d) shows the field distribution of the E_z-component in the x–o–z plane at $\lambda = 5.12$ μm. The E_z field distribution exhibits an antisymmetric form and excites a new mode of graphene nanoribbons.

Fig. 4 shows the E_z field distributions of the two graphene arrays in the x–o–y plane at $\lambda = 5.12$ μm. One of two monitors in Fig. 4(a)

is set at 2 nm above the top graphene nanoribbons arrayed in the y-direction, while the other monitor is set at 2 nm above the bottom graphene nanoribbons arrayed in the x-direction. It can be seen in Fig. 4(a) that the localized and anti-symmetric SPPs are excited in the top nanoribbon array. The SPPs field has the largest intensities at nanoribbon boundaries and decays (in x-direction) as it is away from the two boundaries. The SPPs are localized at the two boundaries of each nanoribbon and do not propagate. It is the so-called localized surface plasmon (LSP), which is the result of the confinement of surface plasmon localized in metal–dielectric interfaces of subwavelength objects with strong field confinement. It is not a propagating wave but a localized electromagnetic field distribution on surfaces. Conversely, surface plasmon polaritons (SPPs), as the interaction between electromagnetic wave and collective electron oscillations in a metal–dielectric or air interface, are a type of delocalized surface wave propagating along the interface with perpendicularly subwavelength-scale confinement.

Additionally, the polarities of the field at the two boundaries of each graphene nanoribbon are opposite. However, the E_z field of the bottom graphene nanoribbon array in Fig. 4(b) is the delocalized and a symmetric SPPs boundary mode, which propagates along the x-direction with the wavelength period of ~300 nm. Besides, the SPPs wave has the largest intensities at the two boundaries of each bottom graphene nanoribbon arrayed in the y-direction with opposite polarities.

To illustrate the effect of the relaxation time τ on resonant responses, we simulate situations of the metasurface at different relaxation times as shown in Fig. 5(a). It can be seen that positions of the main dip and the secondary dip are both unchanged. However, the main dip and the secondary dip both become deeper when the relaxation time τ increases, and the variation of the narrow induced dip is more obvious than that of the main dip. Thereby, the relaxation time τ has little effect on resonant responses.

Fig. 5(b) presents transmission spectra under different angles θ of incidence. Ones can get that the main dip almost does no change when θ increases from 0° to 30°. Interestingly, the third dip with two splitting peaks appears around $\lambda = 5.28$ μm, for oblique incidence. The secondly dip becomes weaker, while the third dip becomes deeper with the increase of θ. The appearance of the third dip can be attributed to the occurring of an E_z-component at oblique incidence, which is perpendicular to the graphene surface and can excite SPPs. Therefore, the SPPs resonance with the coupling between two non-coplanar and inter-perpendicular graphene nanoribbon arrays produces the third dip with small splitting.

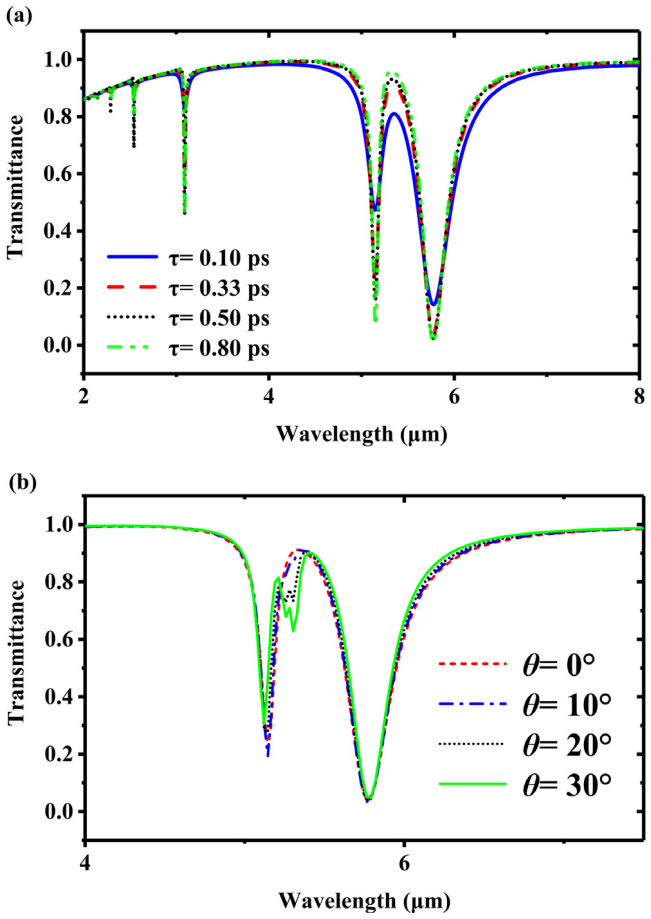

Fig. 5. (a) Transmission spectra at different relaxation times, (b) Transmission spectra of oblique incidences, for the thickness of Al_2O_3 of $H = 40$ nm.

4. Tunable properties of the metasurface with two non-coplanar and inter-perpendicular graphene nanoribbon arrays

As mentioned earlier, Fermi level E_f of graphene can be tuned via applying different gate-voltages, we study the tunable properties of the metasurface with two inter-perpendicular graphene nanoribbon arrays by changing its Fermi level E_f. In the simulation, ambient temperature and scattering probability remain unchanged with the thickness of Al_2O_3 of $H = 40$ nm. Fermi levels of top and bottom graphene nanoribbons are defined as E_{f1}, E_{f2}, respectively. Fig. 6(a) shows the transmission spectra of the graphene metasurface under different Fermi levels. It can be seen that the dip is blue-shifted with Fermi energy of the two arrays increase, which follows the graphene plasmonic resonance wavelength $\lambda \sim 1/E_f^{1/2}$ [33].

To further exploit its tunable properties, we also examined the case of different voltages to top and bottom graphene nanoribbons. As shown in Fig. 6(b), we keep $E_{f2} = 0.5$ eV still and change E_{f1} to study the variation of the transmission spectrum. One can see that the main dip is monotonously blue-shifted when E_{f1} increases from 0.2 eV to 0.8 eV, and achieves a wavelength tuning of 3.91 μm as shown in the inset of Fig. 6(b). Conversely, the position of the induced dip vibrates around its equilibrium position at the wavelength of ~5.30 μm with the increase of E_{f1}, just like a spring. Meanwhile, the depth of the induced dip increases first and then decreases, with the increase of E_{f1}. Then we keep $E_{f1} = 0.5$ eV unchanged and change E_{f2}. One can see in Fig. 6(c) that the position of the main dip also vibrates around at the wavelength of ~5.65 μm, while the induced dip is blue-shifted with the increasing of E_{f2}. Accordingly, it can be concluded that the main dip is mainly controlled by E_{f1}, while the induced dip is mainly controlled by E_{f2}.

Finally, as applications to optical switch and variable optical attenuator (VOA), the optical response of the graphene metasurface with the changing of Fermi level E_f is investigated. To quantitatively evaluate the performances of optical switch and VOA working at narrow band, we set the operation light wavelength of $\lambda = 6.37$ μm, and other material parameters are unchanged. As shown in Fig. 7, when Fermi level E_f, increases from 0.34 eV to 0.40 eV, the transmittance and its corresponding loss varies monotonously from 0.90 and 0.44 dB (defined On-state) to 0.045 and 13.47 dB (defined Off-state), respectively, with the dynamic range of loss around 13 dB. Obviously, the loss range can be adjusted by selecting different working wavelengths. Therefore, the graphene metasurface can be built as an on–off optical switch by simply changing the Fermi level from $E_f = 0.34$ eV into $E_f = 0.40$ eV. Furthermore, by tuning the Fermi level continuously, the graphene metasurface can achieve the function of variable optical attenuator with the dynamic range of attenuation around 13 dB.

5. Conclusion

We have proposed a tunable metasurface based on two non-coplanar and inter-perpendicular graphene nanoribbon arrays in the terahertz and mid-infrared frequencies. The coupling between localized graphene

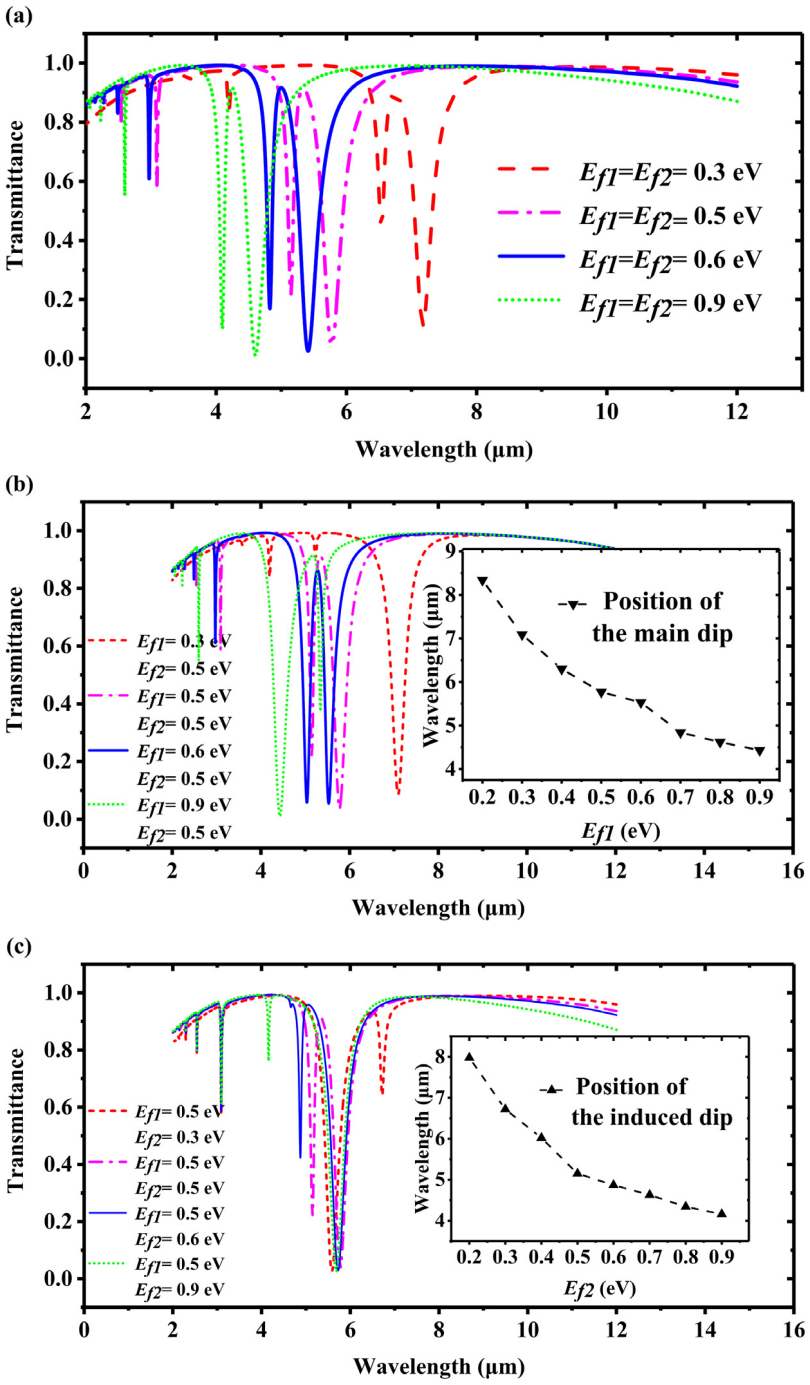

Fig. 6. (a) Transmission spectra of the graphene metasurface at different Fermi levels. (b) Transmission spectra of the graphene metasurface at different top-layer Fermi levels of E_{f1}, given E_{f2} = 0.5 eV. The inset is positions of the main dip at different top-layer Fermi levels of E_{f1}. (c) Transmission spectra of the graphene metasurface at different bottom-layer Fermi levels of E_{f2}, given E_{f1} = 0.5 eV. The inset is positions of the induced dip at different bottom-layer Fermi levels of E_{f2}.

SPPs and delocalized graphene SPPs gives rise to an obvious spectral splitting. By changing the separation between the two graphene nanoribbon arrays, the coupling strength of the structure can be effectively controlled. Meantime, the effect of the relaxation time on resonant responses have little effect on resonant responses and different angles of incidence can change the plasmonic resonance. We have also analyzed its optical response at different Fermi levels. When the equal Fermi levels of the two arrays increase simultaneously, the main dip and the induced dip are both blue-shifted. Additionally, when Fermi levels of the two arrays are separately adjusted, the main dip is mainly controlled by the Fermi level of top graphene nanoribbons, and the induced dip is mainly controlled by the Fermi level of bottom graphene nanoribbons. Two applications of the graphene metasurface, a simple optical switch and a variable optical attenuator with the dynamic range of loss around 13 dB, have been presented. The proposed structure can be potentially used in the research of surface plasmon optoelectronics devices, showing promise in future graphene metasurface optics.

Funding

Guangdong Natural Science Foundation (2014A030313446); Natural Science Foundation of China (11674109); Program for Changjiang

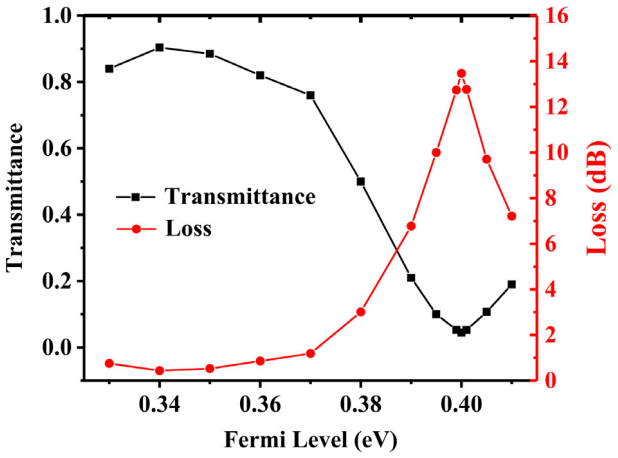

Fig. 7. The dependences of the transmittance and the loss of the metasurface on Fermi level at working wavelength $\lambda = 6.37$ μm.

Scholars and Innovative Research Team in University (NO. IRT13064); Wuhan Morning Light Plan of Youth Science and Technology (2017050304010324).

References

[1] C.M. Soukoulis, M. Wegener, Past achievements and future challenges in the development of three-dimensional photonic metamaterials, Nature Photon. 5 (2011) 523–530.
[2] C.L. Holloway, E.F. Kuester, J.A. Gordon, J. O'Hara, J. Booth, D.R. Smith, An overview of the theory and applications of metasurfaces: The two-dimensional equivalents of metamaterials, IEEE Antennas Propag. Mag. 54 (2) (2012) 10–35.
[3] Z. Li, K. Yao, F. Xia, S. Shen, J. Tian, Y. Liu, Graphene plasmonic metasurfaces to steer infrared light, Sci. Rep. 5 (1) (2015) 12423.
[4] N. Yu, P. Genevet, M.A. Kats, F. Aieta, J.P. Tetienne, F. Capasso, Z. Gaburro, Light propagation with phase discontinuities: Generalized laws of reflection and refraction, Science 334 (6054) (2011) 333–337.
[5] M. Kang, T. Feng, H.T. Wang, J. Li, Wave front engineering from an array of thin aperture antennas, Opt. Express 20 (14) (2012) 15882–15890.
[6] L. Huang, X. Chen, H. Mühlenbernd, G. Li, B. Bai, Q. Tan, G. Jin, T. Zentgraf, S. Zhang, Dispersionless phase discontinuities for controlling light propagation, Nano Lett. 12 (11) (2012) 5750–5755.
[7] A.V. Kildishev, A. Boltasseva, V.M. Shalaev, Planar photonics with metasurfaces, Science 339 (6125) (2013) 1232009.
[8] N. Yu, F. Capasso, Flat optics with designer metasurfaces, Nature Mater. 13 (2) (2014) 139–150.
[9] F. Wang, Y. Zhang, C. Tian, C. Girit, A. Zettl, M. Crommie, Y.R. Shen, Gate-variable optical transitions in graphene, Science 320 (5873) (2008) 206–209.
[10] E.Y. Andrei, G. Li, X. Du, Electronic properties of graphene: A perspective from scanning tunneling microscopy and magnetotransport, Rep. Progr. Phys. 75 (5) (2012) 056501.
[11] N.O. Weiss, H. Zhou, L. Liao, Y. Liu, S. Jiang, Y. Huang, X. Duan, Graphene: An emerging electronic material, Adv. Mater. 24 (43) (2012) 5782–5825.
[12] A. Vakil, N. Engheta, Transformation optics using graphene, Science 332 (6035) (2011) 1291–1294.
[13] K.S. Novoselov, V.I. Falko, L. Colombo, P.R. Gellert, M.G. Schwab, K. Kim, A roadmap for graphene, Nature 490 (7419) (2012) 192–200.
[14] A. Andryieuski, A.V. Lavrinenko, Graphene metamaterials based tunable terahertz absorber: Effective surface conductivity approach, Opt. Express 21 (7) (2013) 9144–9155.
[15] J. Tao, X. Yu, B. Hu, A. Dubrovkin, Q.J. Wang, Graphene-based tunable plasmonic Bragg reflector with a broad bandwidth, Opt. Lett. 39 (2) (2014) 271–274.
[16] L. Ju, B. Geng, J. Horng, C. Girit, M. Martin, Z. Hao, H.A. Bechtel, Xi. Liang, A. Zettl, Y.R. Shen, F. Wang, Graphene plasmonics for tunable terahertz metamaterials, Nat. Nanotechnol. 6 (10) (2011) 630–634.
[17] C. Zeng, J. Guo, X.M. Liu, High-contrast electro-optic modulation of spatial light induced by graphene-integrated Fabry-Pérot microcavity, Appl. Phys. Lett. 105 (12) (2014) 121103.
[18] J. Lao, J. Tao, Q.J. Wang, X.G. Huang, Tunable graphene-based plasmonic waveguides: Nano modulators and nano attenuators, Laser Photonics Rev. 8 (4) (2014) 569–574.
[19] F. Schedin, E. Lidorikis, A. Lombardo, V.G. Kravets, A.K. Geim, A.N. Grigorenko, K.S. Novoselov, A.C. Ferrari, Surface-enhanced Raman spectroscopy of graphene, ACS Nano 4 (10) (2010) 5617–5626.
[20] J. Chen, M. Badioli, P. Alonso-Gonzalez, S. Thongrattanasiri, F. Huth, J. Osmond, M. Spasenovic, A. Centeno, A. Pesquera, P. Godignon, A.Z. Elorza, N. Camara, F.J. Garcia de Abajo, R. Hillenbrand, F.H.L. Koppens, Optical nano-imaging of gate-tunable graphene plasmons, Nature 487 (7405) (2012) 77–81.
[21] J. Tong, M. Muthee, S.Y. Chen, S.K. Yngvesson, J. Yan, Antenna enhanced graphene THz emitter and detector, Nano Lett. 15 (8) (2015) 5295–5301.
[22] J. Tao, Z. Dong, Joel K.W. Yang, Q.J. Wang, Plasmon excitation on flat graphene by s-polarized beams using four-wave mixing, Opt. Express 23 (6) (2015) 7809–7819.
[23] H.-S. Chu, C. How Gan, Active plasmonic switching at mid-infrared wavelengths with graphene ribbon arrays, Appl. Phys. Lett. 102 (23) (2013) 231107.
[24] Z.H. Chen, J. Tao, J.H. Gu, J. Li, D. Hu, Q.L. Tan, F. Zhang, X.G. Huang, Tunable metamaterial-induced transparency with gate-controlled on-chip graphene metasurface, Opt. Express 24 (25) (2016) 29216–29225.
[25] A.Y. Nikitin, F. Guinea, F.J. García-Vidal, L. Martín-Moreno, Edge and waveguide terahertz surface plasmon modes in graphene microribbons, Phys. Rev. B 84 (16) (2011) 161407.
[26] X. Zhu, W. Yan, N.A. Mortensen, S. Xiao, Bends and splitters in graphene nanoribbon waveguides, Opt. Express 21 (3) (2013) 3486–3491.
[27] W. Gao, J. Shu, C. Qiu, Q. Xu, Excitation of plasmonic waves in graphene by guided-mode resonances, ACS Nano 6 (9) (2012) 7806–7813.
[28] X. Yin, T. Zhang, L. Chen, X. Li, Ultra-compact TE-pass polarizer with graphene multilayer embedded in a silicon slot waveguide, Opt. Lett. 40 (8) (2015) 1733–1736.
[29] Edward D. Palik, Handbook of Optical Constants of Solids, Vol. 3, Academic Pres, 1998.
[30] S. Basu, B.J. Lee, Z.M. Zhang, Infrared radiative properties of heavily doped silicon at room temperature, J. Heat Transfer. 132 (2) (2010) 023301.
[31] C. Casiraghi, A. Hartschuh, E. Lidorikis, H. Qian, H. Harutyunyan, T. Gokus, K.S. Novoselov, A.C. Ferrari, Rayleigh imaging of graphene and graphene layers, Nano Lett. 7 (9) (2007) 2711–2717.
[32] Hugen Yan, Xuesong Li, Bhupesh Chandra, George Tulevski, Yanqing Wu, Marcus Freitag, Wenjuan Zhu, Phaedon Avouris, Fengnian Xia, Tunable infrared plasmonic devices using graphene/insulator stacks, Nano Lett. 7 (5) (2012) 330–334.
[33] H. Cheng, S. Chena, P. Yu, X. Duan, B. Xie, J. Tian, Dynamically tunable plasmonically induced transparency in periodically patterned graphene nanostrips, Appl. Phys. Lett. 103 (20) (2013) 203112.